5-2012

SUPERCONDUCTING NaFe1-xCoxAs: CRYSTAL GROWTH, RESISTIVITY, AND SUSCEPTIBILITY MEASUREMENTS

Tucker Netherton
tnethert@utk.edu

SUPERCONDUCTING $NaFe_{1-x}Co_xAs$: CRYSTAL GROWTH, RESISTIVITY, AND SUSCEPTIBILITY MEASUREMENTS

THESIS

Presented to the Faculty of the Department of Physics and Astronomy

in Partial Fulfillment of the Major Requirements

for the Degree of

BACHELOR OF SCIENCE IN

HONORS ACADEMIC PHYSICS

Tucker James Netherton

May 2012

ABSTRACT

$NaFe_{1-x}Co_xAs$ is a Cobalt doped iron-based superconductor (Co-doped FeSC). Compounds with compositions x= 0.0, 0.01, 0.015, 0.02, 0.025, 0.03, 0.04, 0.05, 0.06, 0.1, 0.11, and 0.12 were grown at the University of Tennessee and examined with magnetic susceptibility and resistivity measurements. These measurements were performed to insure compound purity and composition for use in neutron scattering. Antiferromagetic ordering, structural transition, and superconducting behavior under doping are briefly examined for further detail. The data obtained maps the phase diagram for $NaFe_{1-x}Co_xAs$ as a function of doping and is compared to phase diagrams found from previous neutron scattering experiments found in the literature.

SUPERCONDUCTING $NaFe_{1-x}Co_xAs$: CRYSTAL GROWTH, RESISTIVITY, AND SUSCEPTIBILITY MEASUREMENTS

Tucker James Netherton

Signature of Author: Tucker James Netherton

_____

Department of Physics and Astronomy

May, 2012

Advised by:

_____

Dr. Pengcheng Dai

Professor of Physics & Astronomy

Thesis Advisor

Accepted by:

_____

Dr. Soren Sorensen

Dr. Pengcheng Dai

Dr. Marianne Breinig

Physics & Astronomy

TABLE OF CONTENTS

Abstract	ii
List of Figures	v
I. Introduction	1
II. Experimental Methods	5
III. Results	12
IV. Discussion	17
V. Conclusion	18
VI. References	19

LIST OF FIGURES

Figure 1: T_c's for various FeSC's [5].

Figure 2: Dome shaped superconducting phase regions in various FeSC's [2].

Figure 3: Crystal Structures for three different FeSC's [3].

Figure 4: Nuclear and magnetic structures of ideal NaFeAs [7].

Figure 5: Diagram of crucible, Nb tube, and quartz

Figure 6: Large crystal grown in the laboratory.

Figures 7–18: intensity (magnetic moment) vs temperature in units of emu/mol vs K for compositions x= 0.0, 0.01, 0.015, 0.02, 0.025, 0.03, 0.04, 0.05, 0.06, 0.1, 0.11, and 0.12

Figure 19: Compilation I of various compositions, Scott Carr.

Figure 20: Compilation II of various compositions, Scott Carr.

Figure 21: Resistivity measurements of compositions using a PPMS.

Figure 22: Method of T_c determination using tangent lines.

Figure 23: Phase diagram from resistivity measurements, Scott Carr.

Figure 24: Phase diagram from neutron scattering– powder measurements [8].

Figure 25: Temperatures plotted from crystals grown in lab, courtesy of Dr. Guotai Tan.

Figure 26: Phase diagram from resistivity measurements, Scott Carr.

Figure 27: Phase diagram from neutron scattering [7].

INTRODUCTION

Within the past decade, landmark discoveries in iron arsenide systems have prompted further study into the mechanisms and characteristics of high-temperature superconductivity. In addition, growing propensity for investigation has also initiated the creation of many different families of FeSC's (Fe-based superconductors) such as 1111 system RFeFeAs (R= rare-earth), 111 systems NaFeAs and LiFeAs, 122 systems AFe_2As_2 (A= Alkaine earth metals), and 11 Fe-chalcogenide systems. Perhaps the most influential of these compounds was the first FeSC, LaFeAsO, discovered in 2008 [1]. A table compiling many FeSC's and their respective critical temperatures (T_c's), temperatures that signify the temperature at which a compound becomes superconducting, are listed below:

Compound	T_c (K)	References
$LaFeAsO_{0.89}F_{0.11}$	26	[1]
$CeFeAsO_{0.85}$	46.5	[5]
$NdFeAsO_{1-y}$	54	[6]
$SmFeAsO_{1-x}F_x$	55.0	[7]
$Gd_{0.8}Th_{0.2}FeAsO$	56.3	[8]
$LaFePO_{1-x}Fx$	5	[3]
$Ba_{0.6}K_{0.4}Fe_2As_2$	38	[11]
$Sr_{0.6}K_{0.4}Fe_2As_2$	35.6	[19,20]
KFe_2As_2	3.8	[19]
LiFeAs	18	[12–14]
FeSe	8	[16]
$(Sr_4Sc_2O_6)Fe_2P_2$	17	[15]

Figure 1: T_c's for various FeSC's [5].

For most of these systems, varying amounts of electron and hole-doping, isovalent doping, and high pressure induces structural transitions to form a dome-like superconducting region in the phase diagram of these compounds [2]. In addition, the coexistence of

antiferromagnetic (AFM) order and the SC state is observed in the under doped regions of many 111 and 122 systems [3].

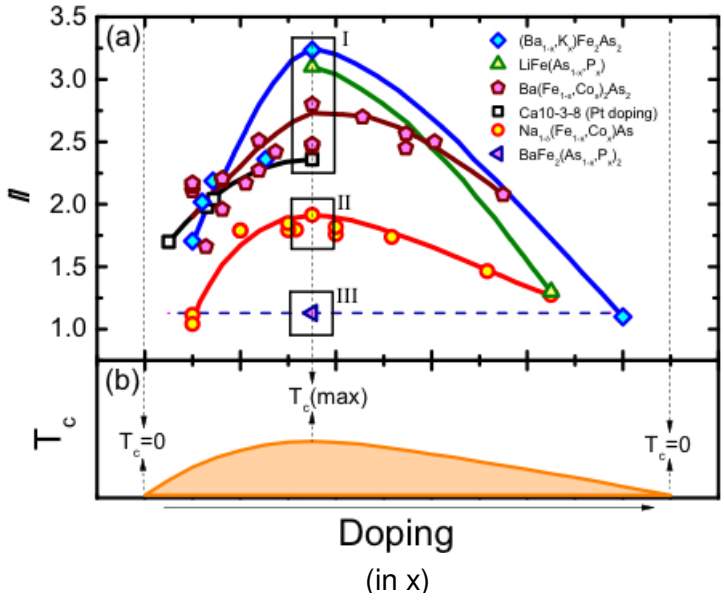

Figure 2: Dome shaped superconducting phase regions in various FeSC's [2].

Also common in the FeSC's are their crystal structures. AFeAs (A= Li, Na), LaFeAsO, and $BaFe_2As_2$ all contain signature FeAs layers with interstitial substances such as Na, Li, LaO, and Ba throughout the lattices of these superconducting metals [3].

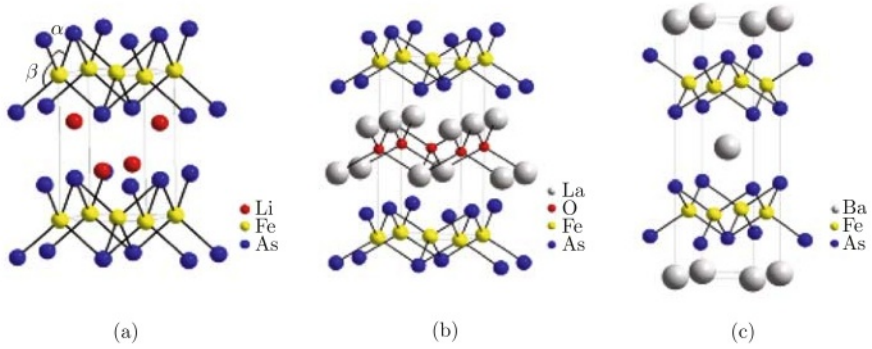

Fig. 1 Crystal structure of **(a)** "111" LiFeAs, **(b)** "1111" LaFeAsO, **(c)** "122" $BaFe_2As_2$.

Figure 3: Crystal Structures for three different FeSC's [3].

BCS theory mandates that the condensation of electrons to form Cooper pairs is the driving mechanism behind conventional superconductivity. This effect involves lattice deformations due to coulomb attractions from these electrons. When doped or under pressure, FeSC's undergo structural deformations in which AF ordering transitions into the SC state. At room temperature, these compounds are tetrahedral, but when temperature is decreased, they undergo structural AF transitions into an orthorhombic state [4]. Thus, the magnetically ordered AF state is suppressed while superconductivity simultaneously emerges under increasing doping [6]. When cooled, the undoped NaFeAs exhibits structural and AF transitions at ~50K and ~40K respectively and exhibits a filamentary SC state at 9K coinciding with AF order [5,6]. The phase diagram of the Co-doped system has also been thoroughly mapped and illustrates the suppression of AF order as bulk superconductivity appears [6].

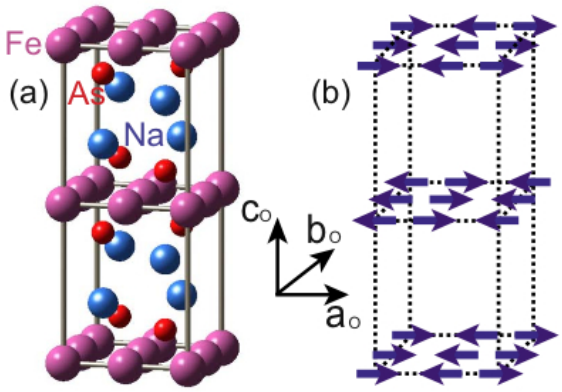

Figure 4: Nuclear and magnetic structures of ideal NaFeAs [7].

Although many doping schemes have been explored within the Fe-based superconductors, NaFeAs and LiFeAs remain to be the only 111 parent compounds [4]. In Dr. Dai's laboratory at the University of

Tennessee, large single crystals of Co-doped NaFeAs have been grown and present significantly less problems in the growth process than NaFeAs crystals with other dopants such as V, Ru, and Ti. Cobalt sits adjacent to Fe in the periodic table and has an atomic size comparable to Fe which makes it ideal to dope into the FeAs layer to replace Fe. In addition, its valence charge is identical to Fe and allows for charge to be balanced within the compound.

To experimentally examine the behavior of the AF and SC phase transitions and superconductivity of $NaFe_{1-x}Co_xAs$, magnetization measurements and resistivity measurements were taken from 12 different nominal dopings to determine the changes of T_c. This study's purpose is to prepare pure, reliable crystals for accurate neutron scattering measurements. However, as an added undertaking, this paper compares the data from the crystal growth and transport measurement process to the findings of many experiments that detail the character of the SC phase under electron doping in Co doped NaFeAs.

EXPERIMENTAL METHODS

$NaFe_{1-x}Co_xAs$ with 12 nominal compositions (x=0.0, 0.01, 0.015, 0.02, 0.025, 0.03, 0.04, 0.05, 0.06, 0.1, 0.11, 0.12) were grown in the lab from elemental materials under an Argon atmosphere.

In order to grow homogenous single crystals of Co-doped NaFeAs, a very detailed procedure was put in place to prepare samples large enough for neutron scattering experiments.

First, compounds are mixed using the flux method inside an Argon glovebox. The accuracy of each component of a compound is known to 0.0001 of a gram. Once weighed on a sensitive scale, the elemental Co, As, and Fe are evenly mixed in powder form while Na is cut into very small pieces in order to maximize the exposed surface area. This will ensure that the contents evenly react when placed under high heat and do not vigorously sublimate while the crystal is being formed. After the components are evenly combined with a total mass of approximately 16g, the mixed compound is placed inside of a porcelain crucible and then sealed inside of a 28mm diameter Niobium container using an arc welder. This layered ensemble is then lowered into a quartz tube, and sealed inside under vacuum using a blowtorch. The quartz layer protects the laboratory from exposure to the sample's contents if the Niobium cylinder were to rupture. It also adds an insulating layer to the sample during heating and cooling.

Figure 5: Diagram of crucible, Nb tube, and quartz

Figure 6: Large crystal grown in the laboratory.

The compound is initially heated to solidify the contents, release excess heat, and make the contents more uniformly distributed in a process called pre-sintering. Pre-sintering takes place in a large, 1500°C high-temperature oven that is programmed in a stepwise fashion to gradually heat the compound. Nine compounds at a time are slowly heated in intervals to reach 830C, held at that temperature for 10 hours, and slowly cooled to room temperature. The compounds are then sintered one by one in a high temperature insulated furnace for many hours in a similar stepwise fashion. The sintering process safeguards against dangerous fumes escaping by placing the furnace under a closed fume hood during heating. After sintering, the condition of the quartz and Niobium are examined to see if oxidation has occurred. Oxidation signifies that air has reacted with the compound and changed the chemical composition of the compound. This happens if the compound is incorrectly mixed, welded, or sealed and must be remade inside the argon atmosphere.

After the successful growth of a homogenous crystal, the compound is weighed and coated in synthetic non-Hydrogen containing glue. This glue coats the surface of the crystal and minimizes oxidation while the compound is transferred from an argon atmosphere to the PPMS for magnetization measurements. If these compounds were exposed to oxygen and moisture, they would almost completely sublimate due to the highly reactive elemental sodium in the compound’s crystal structure.

Magnetic susceptibility and resistivity were measured for each of the doped, single crystal compounds and were examined using a Quantum Design Model 6000 Physical Property Measurement System (PPMS).

RESULTS

Each resulting plot below was obtained from measurements of magnetic susceptibility. Dr. Guotai Tan, Dr. Chenglin Zhang, graduates students Scott Carr and Yu Song, and myself carried out these measurements. They were measured at the University of Tennessee, Oak Ridge National Laboratory, and Beijing Normal University using a PPMS. The single plots were graphed using graphing software from data imported directly from the instrument. For each of the compounds, a single crystal was cooled in a zero-field environment and measured

under a field of 10Oe from 2K to 25K. The values for this graph are intensity (magnetic moment) vs temperature in units of emu/mol vs K.

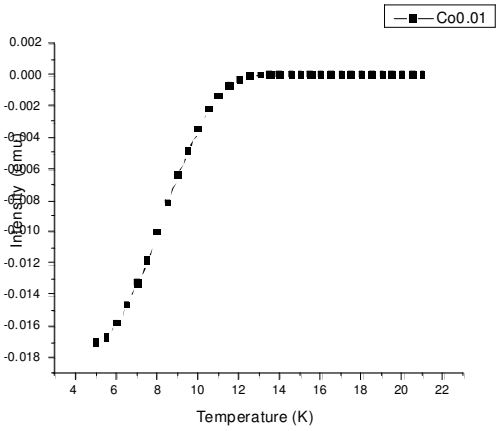

Figure 7.

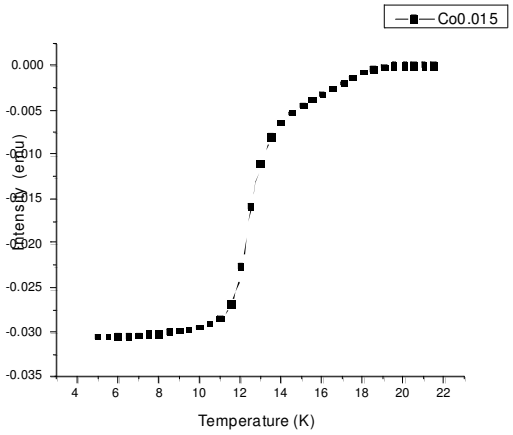

Figure 8.

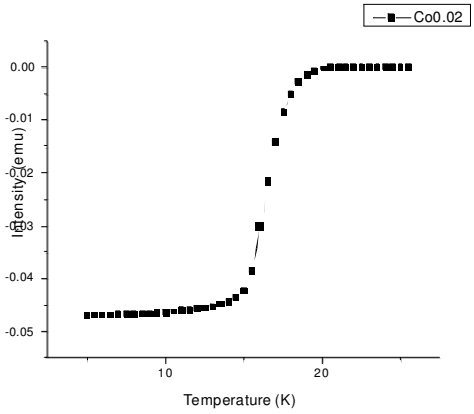

Figure 9.

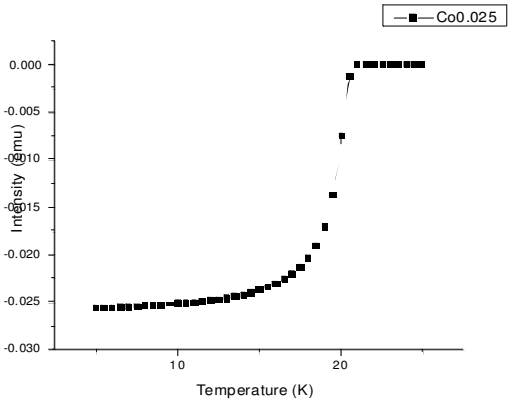

Figure 10.

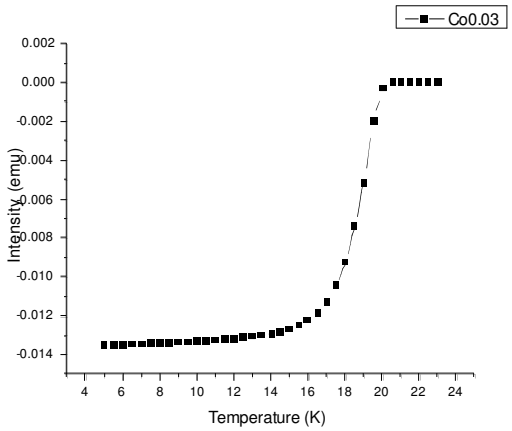

Figure 11.

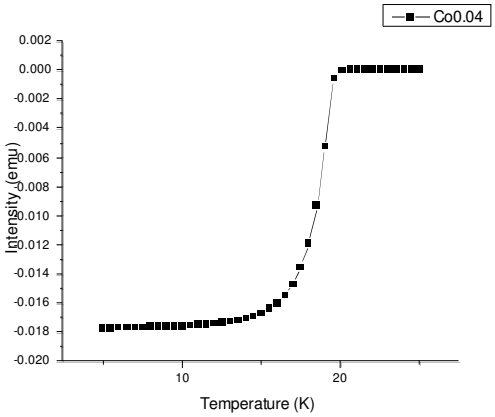

Figure 12.

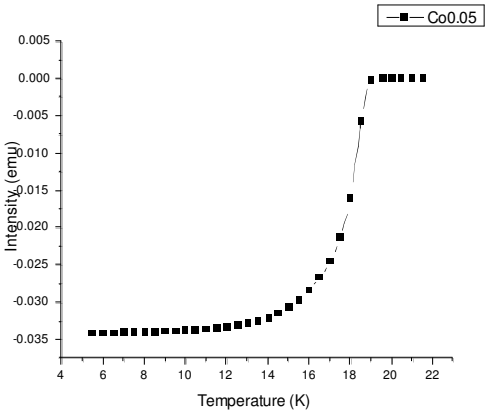

Figure 13.

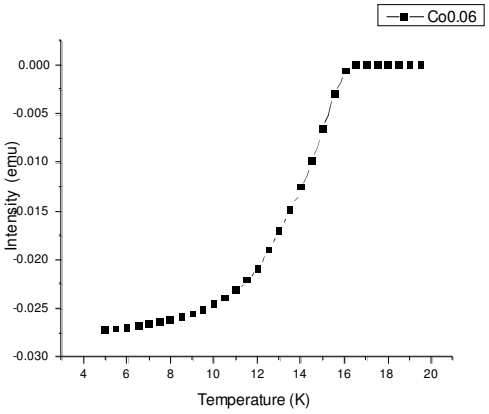

Figure 14.

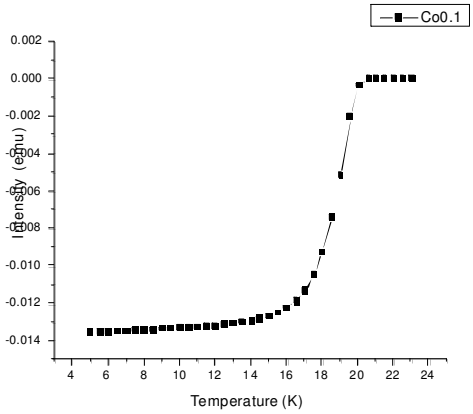

Figure 15.

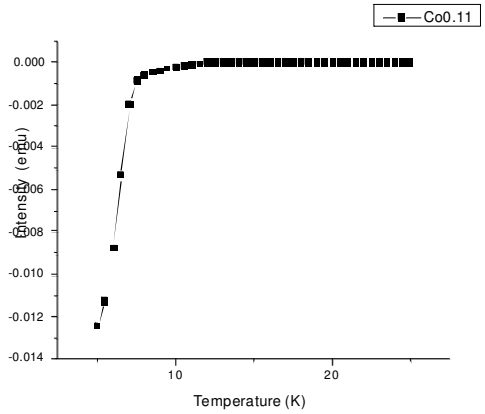

Figure 16.

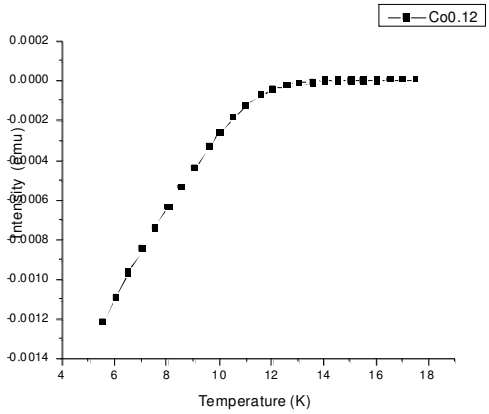

Figure 17.

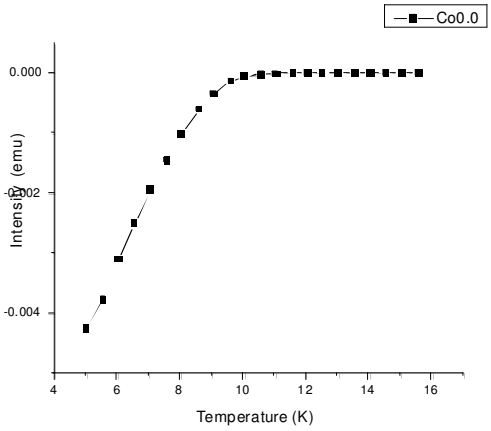

Figure 18.

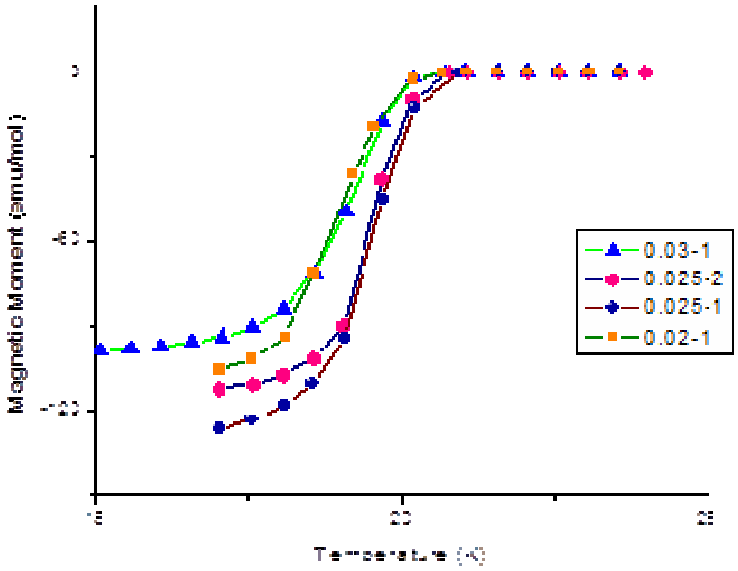

Figure 19: Compilation I of various compositions.

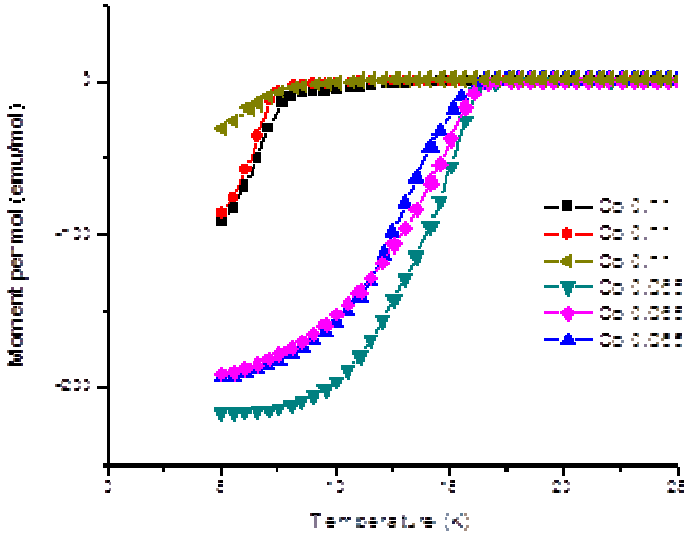

Figure 20: Compilation II of various compositions.

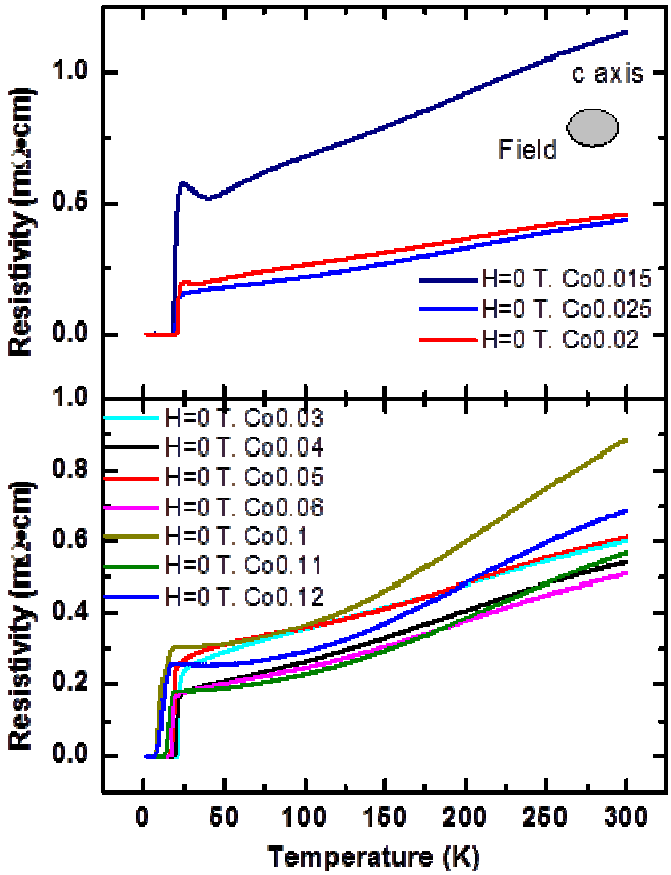

Figure 21: Resistivity measurements of compositions using a PPMS, courtesy of Dr. Guotai Tan.

Discussion

The T_c for every superconducting compound occurs when the substance repels all external magnetic fields and becomes diamagnetic. In the graph below, a dramatic slope is seen below 20K. Ideally, in a compound that is completely superconducting (with no stoichiometric impurities), this slope would drop off steeply and without much transition from higher temperatures. A gradual drop off from higher temperatures close to T_c implies that the compound is impure and that in different regions, the compound became superconducting at different temperatures due to structural or chemical variation. As illustrated below, a simple graphical method was put in place to systematically ascribe T_c temperatures to each susceptibility graph.

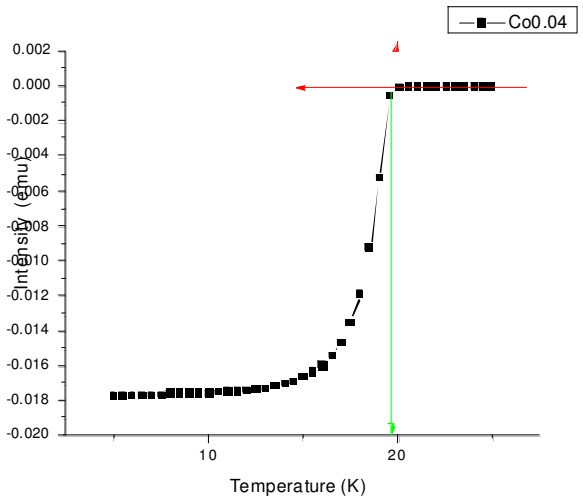

Figure 22: Method of Tc determination using tangent lines.

Two tangent curves were fitted to each plot, each lying tangent to the slopes approaching T_c from both directions. The horizontal axis value (temperature K) of the intersection of these two curves is the recorded T_c (Figure 22). These measurements attest to the homogeneity of the compounds as well as their application for additional measurements. Susceptibility measurements are most useful to obtain T_c's and composition purity.

The same compounds utilized for the susceptibility measurements were also used for resistivity measurements. While in the superconducting state, superconducting compounds have an ideal resistance of zero Ohms. This region of zero slope is seen at varying temperatures close to 20 K in figure 21. To determine the Neel temperatures (Tn), temperatures of structural transition (Ts), and T_c, analysis of the slopes of resistivities from figure 21 can be utilized. By finding the maximum of the first derivate for each compound, the horizontal value of the slope will result in the T_c. This is so due to the fact that the steep transition from superconducting

to insulating/semi-conducting behavior results in a large, identifiable maximum when the slope is plotted. Using these values, a phase diagram as constructed. Other structural transitions are also identified from the graph of the slope.

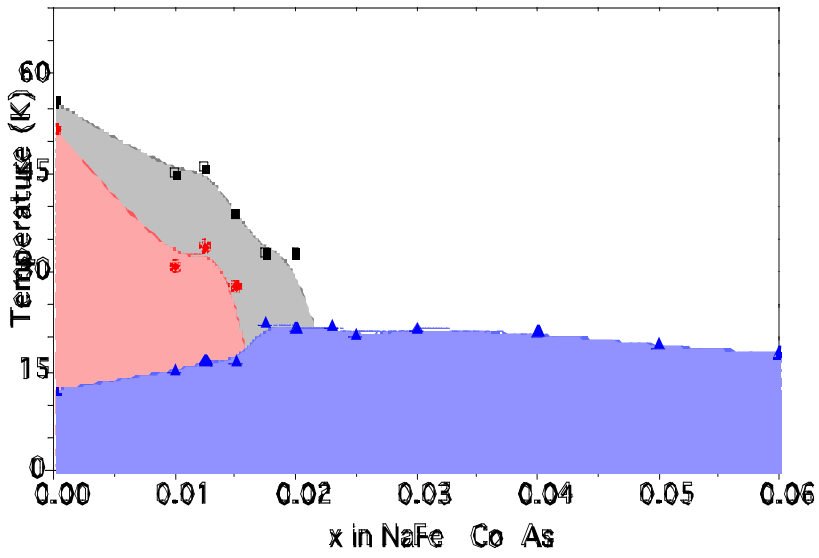

Figure 23: Phase diagram from resistivity measurements.

This phase diagram in Figure 23 identifies the AF region in red with red points corresponding to Neel temperatures. The grey region corresponds to an area of structural transition with black points corresponding to structural transition temperatures. The blue region corresponds to the superconducting state in which the nominal doping of each compound is represented by blue triangles. Thus, the phase diagram illustrates important behavior surrounding magnetic ordering, structural transition, and superconductivity as a function of doping.

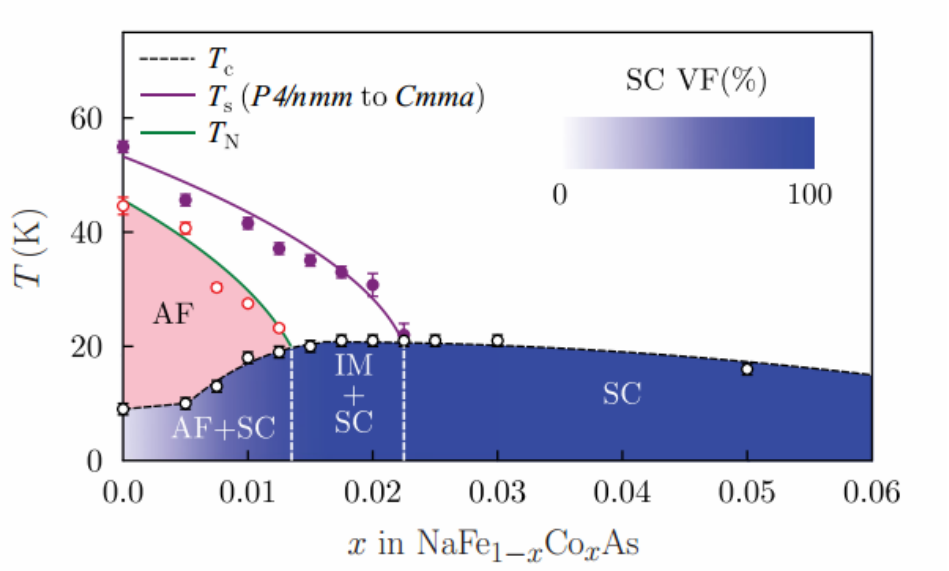

Figure 24: Phase diagram from transport and powder measurements [8].

While the compounds are not stoichiometrically verified, their properties and Tc's testify to the compounds' consistencies within the scope of the measurements. This is shown through the similarities of the phase diagram from other transport and powder measurements in figure 24. As seen in figures 23 and 24, the separate AF, SC, and structural transition regions exhibit similar behavior. With less doping, AF and SC behavior coexist; with more doping, the SC state becomes more maintained at higher temperatures reaching to ~20K.

The temperatures reported in (Figure 24) are higher than the temperatures from figure 23, but more similar to values found in susceptibility measurements found from Figures 7-18. The differences between the reported temperatures from the measurements grown from the single crystal compounds grown in Dr. Dai's lab are plotted below in figure 25.

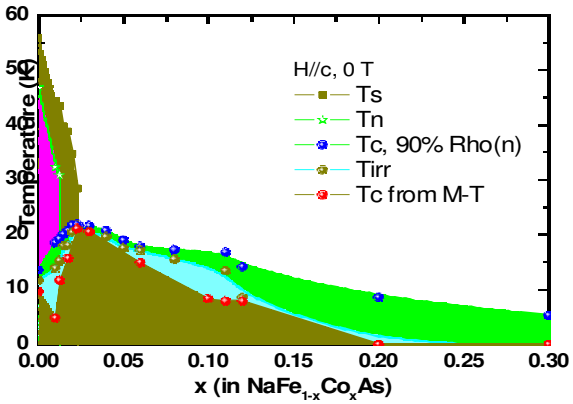

Figure 25: Temperatures plotted from crystals grown in lab, courtesy of Dr. Guotai Tan.

Susceptibility measurements are reported as (Tc from M-T) in red, resistivity measurements (Tc, 90% Rho(n) are in blue. Except near optimum doping of x= 0.025, the values for resistivity are similar to those from susceptibility measurements.

However, after optimum doping there is a growing discrepancy between the T_c measurements as x increases in doping. The gap between the Tc's, for example, at x=0.20, is due to the fact that the susceptibility measurements measure a bulk effect, while the resistivity measurements measure a microscopic effect. During resistivity measurements, any electrons due to tunneling are detected, even if most of the compound is no longer in the superconducting state. The PPMS is not able to detect magnetic moments comparable to this scale and accounts for the discrepancy between the susceptibility and resistivity measurements.

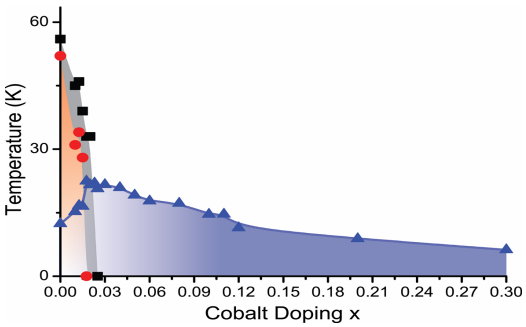

Figure 26: Phase diagram from resistivity measurements.

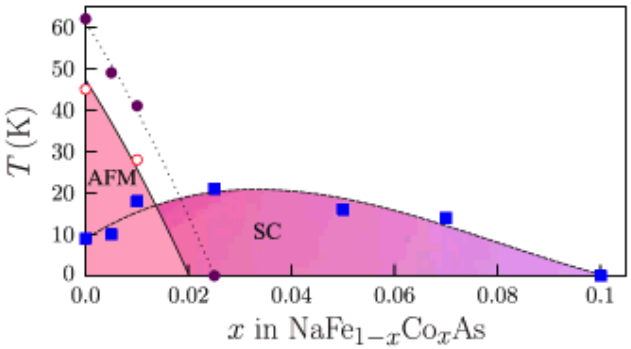

Figure 27: Phase diagram from neutron, muon, and synchrotron techniques [6].

Further evidence for commonalities exhibited by these diagrams in the literature can be seen above in figures 26 and 27. This compiled data from resistivity measurements closely resembles the phase diagram found through neutron, muon, and synchrotron techniques and show how magnetic ordering and the superconducting state behave as a function of doping [6].

CONCLUSIONS

This paper has compiled data used to insure proper compound growth for neutron scattering experiments on single crystals. From the trends observed in the magnetic susceptibility measurements, each homogeneous compound exhibits differences between T_c as a function of doping. While differences in reported T_c's from resistivity and susceptibility measurements exist due to quantum vs. bulk detective capabilities, the phase diagrams of both preserve the general behavior of the phase transitions under doping. The behavior of the SC phase, AF ordering, and structural transition is illustrated in Figure 25 from both resistivity and susceptibility measurements and show common trends to experiments found in the literature.

References

1. Kamihara Y, Watanabe T, Hirano M, Hosono H. 2008. J. Am. Chem. Soc. 130:3296–97

2. K. Cho, M. A. Tanatar, N. Spyrison, H. Kim, G. Tan, Prozorov R., et al., arXiv:1201.2966v1.

3. Wang. Front. Phys. China, 2009, 4(4): 464–468 (2009).

4. D. C. Johnston, Advances in Physics **59**, 803 (2010).

5. G. F. Chen *et al.*, Phys. Rev. Lett. **102**, 227004 (2009).

6. Dinah R. Parker *et al.*, arXiv:0909.0417v2.

7. Shiliang Li, et. Al., Physical Review B **80**, 020504(R)(2009).

8. J.D. Wright, et. Al., arXiv:1112.0419v1.

Acknowledgments

For help with data and figures, Dr. Guotai Tan, Dr. Chenglin Zhang, Scott Carr, Song Yu, Miaoyin Wang.